The Angstrom Exponent and Bimodal Aerosol Size Distributions

Gregory L. Schuster

NASA Langley Research Center, Hampton, VA, USA

Oleg Dubovik

NASA Goddard Space Flight Center, Greenbelt, Maryland, USA

Brent N. Holben

NASA Goddard Space Flight Center, Greenbelt, Maryland, USA

Gregory L. Schuster

NASA Langley Research Center

Hampton, Virginia, USA 23681

gregory.l.schuster@nasa.gov

Abstract.

Powerlaws have long been used to describe the spectral dependence of aerosol extinction, and the wavelength exponent of the aerosol extinction powerlaw is commonly referred to as the Angstrom exponent. The Angstrom exponent is often used as a qualitative indicator of aerosol particle size, with values greater than two indicating small particles associated with combustion byproducts, and values less than one indicating large particles like sea salt and dust. In this study, we investigate the relationship between the Angstrom exponent and the mode parameters of bimodal aerosol size distributions using Mie theory calculations and Aerosol Robotic Network (AERONET) retrievals. We find that Angstrom exponents based upon seven wavelengths (0.34, 0.38, 0.44, 0.5, 0.67, 0.87, and 1.02 μm) are sensitive to the volume fraction of aerosols with radii less then 0.6 μm, but not to the fine mode effective radius. The Angstrom exponent is also known to vary with wavelength, which is commonly referred to as curvature; we show how the spectral curvature can provide additional information about aerosol size distributions for intermediate values of the Angstrom exponent. Curvature also has a significant effect on the conclusions that can be drawn about two-wavelength Angstrom exponents; long wavelengths (0.67, 0.87 μm) are sensitive to fine mode volume fraction of aerosols but not fine mode effective radius, while short wavelengths (0.38, 0.44 μm) are sensitive to the fine mode effective radius but not the fine mode volume fraction.

1. Introduction

Knowledge of the aerosol optical thickness (AOT) throughout much of the shortwave spectral region (∼0.3–5 μm) is necessary to compute the shortwave aerosol radiative forcing at the surface and the top of the atmosphere. The AOT is easily measured in discrete spectral intervals with sunphotometers located at the surface, but gas and water vapor absorption prevent the measurement of AOT at all wavelengths of interest. This difficulty is easily circumvented because *Angstrom* [1929] noted that the spectral dependence of extinction by particles may be approximated as a powerlaw relationship:

$$\tau(\lambda) = \tau_1 \lambda^{-\alpha}, \tag{1}$$

where $\tau(\lambda)$ is the aerosol optical thickness (AOT) at the wavelength λ, τ_1 is the approximated AOT at a wavelength of 1 μm sometimes called the turbidity [*Angstrom*, 1964], and α has come to be widely known as the Angstrom exponent.

In addition to being a useful tool for extrapolating AOT throughout the shortwave spectral region, the value of the Angstrom exponent is also a qualitative indicator of aerosol particle size [*Angstrom*, 1929]; values of $\alpha \lesssim 1$ indicate size distributions dominated by coarse mode aerosols (radii $\gtrsim 0.5\,\mu$m) that are typically associated with dust and sea salt, and $\alpha \gtrsim 2$ indicating size distributions dominated by fine mode aerosols (radii $\lesssim 0.5\,\mu$m) that are usually associated with urban pollution and biomass burning [*Eck et al.*, 1999; *Westphal and Toon*, 1991]. *Kaufman et al.* [1994] demonstrated that the Angstrom exponent can be a good indicator of the fraction of small particles with radii $r = 0.057$–$0.21\,\mu$m relative to larger particles with radii $r = 1.8$–$4\,\mu$m for tropospheric aerosols.

Since the Angstrom exponent is easily measured using automated surface sunphotometry [*Holben et al.*, 1998] and is becoming increasingly accessible to satellite retrievals [*Nakajima and Higurashi*, 1998; *Higurashi and Nakajima*, 1999; *Deuze et al.*, 2000; *Ignatov and Stowe*, 2002; *Jeong et al.*, 2005], the true utility of this parameter lies in its empirical relationship to the aerosol size distribution. For instance, α has been used to characterize the maritime aerosol component at island sites [*Kaufman et al.*, 2001; *Smirnov et al.*, 2002, 2003], biomass burning aerosols in South America and Africa [*Dubovik et al.*, 1998; *Reid et al.*, 1999; *Eck. et al.*, 2001b, 2003], and urban aerosols in Asia [*Eck. et al.*, 2001a]. Measurements also indicate that the Angstrom exponent varies with wavelength, and that the spectral curvature of the Angstrom exponent contains useful information about the aerosol size distribution [*King and Byrne*, 1976; *King et al.*, 1978; *Eck et al.*, 1999; *Eck. et al.*, 2001a, b, 2003; *Kaufman*, 1993; *O'Neill and Royer*, 1993; *O'Neill et al.*, 2001a, b, 2003; *Villevalde et al.*, 1994].

The focus of this paper is to explore the relationship between the spectral dependence of extinction and the size distribution of atmospheric aerosols. We begin by illustrating the sensitivity of α to the median radius of monomodal aerosol size distributions, using multi-wavelength Mie calculations of $\tau(\lambda)$ for 38 monomodal lognormal aerosol size distributions. Then we explore the relationship between α and 45 bimodal lognormal aerosol size distributions, demonstrating that α is more sensitive to the fine mode volume fraction than the fine mode median radius. Next, we apply the same technique to explore the information content in the wavelength-dependence of α (i.e., the curvature of α). Finally, we discuss application of the Angstrom exponent and the spectral curvature for setting limits on the possible size distributions associated with aerosol optical depth measurements.

Before proceeding further, however, a word about the origination of the term "Angstrom exponent" is in order. The term "Angstrom exponent" originates from an early treatise by Anders Angstrom that provides the first documentation of Equation (1) currently available in english [*Angstrom*, 1929]. However, that article cites an even earlier laboratory study whereby Lundholm documented the powerlaw relationship for the absorption of thin powders at Uppsala in 1912, prompting at least one author to point out that we are honoring the wrong person [*Bohren*, 1989]. Unfortunately, the Lundholm citation in *Angstrom* [1929] is obscure and perhaps incorrect, as our library staff was unable to locate it. Compounding matters even further, it is not even clear whether Lundholm or Lindholm documented the powerlaw in 1912, as *Angstrom* [1929] uses both forms of spelling. Our library staff did find references to a F. Lindholm at Uppsala in *Science Abstracts*, but none of the abstracts mention the spectral dependence of particulate extinction. Subsequent references to Lundholm and Lindholm on this topic have not appeared in the atmospheric literature, and Angstrom claimed full credit for introducing the methods of evaluating atmospheric turbidity parameters in later articles [*Angstrom*, 1930, 1961, 1964]. So who should get the credit for originating and promoting Equation (1)? After presenting the discussion above, we maintain the standard nomenclature. Angstrom admittedly did not originate the empirical powerlaw, but he did publish at least four articles documenting the relationship between α and particle size; meanwhile, we are unable to obtain any public documentation of Equation (1) by Lundholm or Lindholm, making it impossible for us to fairly evaluate this person's contribution.

2. Extinction Calculations

Atmospheric aerosols are never limited to a single particle size, so we seek realistic polydisperse aerosol size distributions for our calculated values of τ. Although *Angstrom* [1929] documented the relationship between the Angstrom exponent and single particle sizes, *Junge* [1955] was the first to explore a relationship between the Angstrom exponent and polydisperse aerosol size distributions. By assuming a powerlaw relationship for the number density (N) of aerosols as a function of radius (r):

$$\frac{dN(r)}{d\log(r)} = Ar^{-\nu}, \tag{2}$$

where A and ν are the coefficients that characterize the size distribution, *Junge* [1955] was able to show that $\nu \approx \alpha + 2$ for nonabsorbing aerosols with $\alpha > 1$ (see also *Junge* [1963]). The simplicity of this relationship has found widespread appeal, and the "Junge distribution" has subsequently appeared in numerous textbooks [*McCartney*, 1976; *Measures*, 1984; *Stephens*, 1994; *Seinfeld and Pandis*, 1998; *Pruppacher and Klett*, 1997]. However, the simple relationship $\nu \approx \alpha + 2$ does not hold for small values of α ($\alpha \lesssim 1$) or for absorbing aerosols [*Junge*, 1955; *Tomasi et al.*, 1983; *Cachorro et al.*, 1993; *Cachorro and de Frutos*, 1995], and the Junge powerlaw distribution is mainly of historical interest.

Subsequent research has shown that Equation (2) does not accurately describe atmospheric aerosol size distributions, and that multimodal lognormal distributions are more appropriate [*Davies*, 1974; *Whitby*, 1978; *Ott*, 1990]:

$$\frac{dV(r)}{d\ln r} = \sum_{i=1}^{n} \frac{C_i}{\sqrt{2\pi}\sigma_i}, \exp\left[\frac{-(\ln r - \ln R_i)^2}{2\sigma_i^2}\right], \tag{3}$$

where C_i represents the particle volume concentration, R_i is the median or geometric mean radius, σ_i is the variance or width of each mode, and n is the number of lognormal

aerosol modes. Here, we have switched to the volume concentration $dV(r) = 4/3\pi r^3 dN(r)$ because the optical effects of atmospheric aerosols are more closely related to their volume than their number [*Whitby*, 1978; *Seinfeld and Pandis*, 1998]. *Whitby* [1978] observed thousands of aerosol size distributions, and found that most could be described with three volumetric modes: a nuclei mode with geometric mean radii of 0.0075–0.020 μm, an accumulation or fine mode with geometric mean radii of 0.075–0.25 μm, and a coarse particle mode with geometric mean radii of 2.5–15 μm. An additional mode with a geometric mean radius of $\sim$0.5 μm was observed by *Kaufman et al.* [1994] after the Mt. Pinatubo volcanic eruption in June, 1991; they attributed this mode to the stratospheric aerosol loading at that time.

We can use Equation (3) to calculate the extinction of a polydisperse distribution of aerosols with refractive index m in an atmospheric column of height Z:

$$\tau(\lambda) = \int \frac{3Q_{ext}(m, r, \lambda)}{4r} \frac{dV}{d\ln r}\, d\ln r\, dZ, \tag{4}$$

where Q_{ext} is the extinction efficiency, which we calculate exactly for spherical aerosols using Mie theory [*Wiscombe*, 1980]. The extinction is sensitive to the size of the particles in the distribution, which we illustrate at two wavelengths in Figure 1 for monomodal size distributions with variable median radii, but identical mass and width. (Here, we have plotted the results in terms of the mean effective radius (R_{eff}) of the size distribution, which we define below). Note that the fine mode particles ($R_{eff} \lesssim 0.25\,\mu$m) have a much greater effect on the AOT at the visible wavelength (0.5 μm) than at the near infrared wavelength (1.0 μm). Likewise, the coarse mode particles ($R_{eff} \gtrsim 2\,\mu$m) provide similar contributions to the AOT at both wavelengths in this example. The nuclei mode ($0.0075\,\mu\text{m} \lesssim R_{eff} \lesssim 0.020\,\mu\text{m}$) contributes very little to the AOT at both wavelengths,

so we do not calculate the optical effect of this mode for the remainder of this article. We show in later sections that the interplay of the aerosol optical depth at the visible and near infrared wavelengths with the fine and coarse mode particles provides information about the aerosol size distribution.

We use the effective radius throughout this article, which is defined as the average radius weighted with the geometrical cross-sectional area [*Hansen and Travis*, 1974],

$$R_{eff} = \frac{\int_0^\infty r\pi r^2 \frac{dN}{d\ln r} d\ln r}{\int_0^\infty \pi r^2 \frac{dN}{d\ln r} d\ln r}, \tag{5}$$

and is often used for calculations involving droplet size distributions. This is because spherical drops scatter radiation in proportion to their geometrical cross-sectional area (πr^2), so the single-scatter properties of size distributions are more closely related to the effective radius than to the median radius [*Hansen and Travis*, 1974; *Liou*, 1992; *Mishchenko et al.*, 1997]. This is useful because the nomenclature for describing lognormal aerosol size distributions is not universal, and size distributions with the same effective radius and the same effective variance will have similar single-scatter albedos [*Mishchenko et al.*, 1997]. The relationship between the effective radius and the median radius for monomodal size distributions ($n = 1$ in Equation 3) is shown for three mode widths in Figure 2.

3. Spectral dependence of τ

In practical applications, the extinction of atmospheric particles are measured at two or more wavelengths in the ultraviolet, visible, or near infrared spectral regions and the Angstrom exponent is calculated from the slope of the linear regression of the logarithm

of Equation (1), viz:

$$\ln \tau(\lambda_i) = \ln \tau_1 - \alpha \ln \lambda_i, \tag{6}$$

where the subscript i emphasizes that the measurements are obtained at discrete wavelengths. The measurement wavelengths are chosen to avoid spectral regions with significant gas absorption, although spectral regions with some ozone absorption may be used by including a compensating adjustment. Measurements are typically obtained with narrowband wavelength filters that are about 10 nm wide and span the 0.3–1.1 μm spectral response region of silicone photodetectors [*Shaw et al.*, 1973].

The Angstrom exponent itself varies with wavelength, and a more precise empirical relationship between aerosol extinction and wavelength is obtained with a 2nd-order polynomial [*King and Byrne*, 1976; *Eck et al.*, 1999; *Eck. et al.*, 2001a, b, 2003; *Kaufman*, 1993; *O'Neill et al.*, 2001a, 2003]:

$$\ln \tau(\lambda_i) = a_0 + a_1 \ln \lambda_i + a_2 (\ln \lambda_i)^2. \tag{7}$$

Here, the coefficient a_2 accounts for a "curvature" often observed in sunphotometry measurements. Note that for the special case of $a_2 = 0$, the coefficients a_0 and a_1 equate to $a_0 = \ln \tau_1$ and $a_1 = -\alpha$.

Some authors have noted that the curvature is also an indicator of the aerosol particle size, with negative curvature indicating aerosol size distributions dominated by the fine mode and positive curvature indicating size distributions with a significant coarse mode contribution [*Kaufman*, 1993; *Eck et al.*, 1999; *Eck. et al.*, 2001b; *Reid et al.*, 1999]. This is illustrated graphically in Figure 3, which shows the spectral dependence of extinction for two plausible aerosol size distributions that have the same Angstrom exponent of $\alpha = 2$. The AOT with negative curvature was calculated for a monomodal size distribution

with a median radius of $R = 0.12\,\mu$m to characterize a fine mode distribution, and the AOT with positive curvature was calculated for a bimodal aerosol size distribution with a significant coarse component of $C_{crs}/(C_{fine} + C_{crs}) = 0.4$. The negative curvature associated with the monomodal aerosol size distribution is a natural byproduct of the Mie calculation, and is typical of the accumulation mode sizes common to atmospheric aerosols. Positive curvature occurs for the bimodal distribution because the coarse mode AOT at the near-infrared wavelengths is a much greater fraction of the visible AOT than the same ratio induced by fine mode aerosols. That is, AOT($\lambda = 1\,\mu$m)/AOT($\lambda = 0.5\,\mu$m) at $R_{eff} = 2\,\mu$m is much greater than AOT($\lambda = 1\,\mu$m)/AOT($\lambda = 0.5\,\mu$m) at $R_{eff} = 0.1\,\mu$m (see Figure 1, for example). We discuss this further in Sections 4 and 5.

4. Response of α to changes in polydisperse aerosol parameters

We study the impact of particle size on the spectral variability of extinction by calculating $\tau(\lambda)$ for a variety of plausible aerosol size distributions (via Equation 4). That is, we test the sensitivity of the empirical coefficients α, a_1, and a_2 (in Equations 6 and 7) to the variability of the parameters of bimodal aerosol size distributions C_i, R_i, σ_i (in Equation 3), using exact calculations of $\tau(\lambda)$ at seven wavelengths (0.34, 0.38, 0.44, 0.5, 0.67, 0.87, and 1.02 μm). We normalize the aerosol optical depth at $\lambda = 0.44\,\mu$m by scaling $\frac{dV}{d\ln r}$, but note that our computations of α, a_1, and a_2 are independent of this scale factor. This would not be the case for real atmospheric measurements, where the determination of these empirical coefficients at low optical depths could be altered because of instrument accuracy and resolution.

4.1. Monomodal aerosol size distributions

We begin by calculating the Angstrom exponent (α) for a set of spherical monomodal aerosol size distributions with a variety of median radii ($R_i = 0.04$ to $7\,\mu$m). We chose two widths for our monomodal size distributions consistent with the fine and coarse modes in the climatology of *Dubovik et al.* [2002]: $\sigma = 0.38$ for median radii $R_i \leq 0.6\,\mu$m, and $\sigma = 0.75$ for median radii $R_i \geq 0.6\,\mu$m. We simulated an internal aerosol mixture for our distributions, tuning the volume fractions of water, ammonium sulfate, and black carbon until we achieved a minimum χ^2 fit to a refractive index of $m = 1.37 - 0.003i$ at four wavelengths: 0.44, 0.67, 0.87, and 1.02 μm [*Schuster et al.*, 2005]. This technique results in a plausible aerosol mixture with a spectrally variable refractive index. We use linear regression of Equation (6) to calculate the associated empirical Angstrom exponents. The sensitivity of the Angstrom exponent to the effective radius of the size distribution is shown in Figure 4a. Although we show two different mode widths (σ) for the small and large effective radii in this test in order to maintain values similar to the *Dubovik et al.* [2002] climatology, the results are qualitatively the same for either mode width at all effective radii; that is, a marked decrease in the Angstrom exponent for particles smaller than about 0.6 μm and relatively little sensitivity to larger particles [*Cachorro et al.*, 2000].

Figure 4a indicates that the Angstrom exponent is quite sensitive to the effective radius of size distributions that are consistent with fine mode aerosols ($R_{eff} \lesssim 0.25\,\mu$m), but provides little information about the effective radius of coarse monomodal aerosols (as evidenced by the nearly constant value shown for $R_{eff} \gtrsim 2\,\mu$m). This is because the spectral variability of extinction diminishes for particles larger than the incident wavelength

(i.e., the visible and near infrared AOTs in Figure 1 are nearly equivalent for coarse mode particles). Nonetheless, the low α associated with coarse mode aerosols can significantly reduce the Angstrom exponent when they are included in bimodal aerosol size distributions. We explore the impact of coarse mode aerosols on the Angstrom exponent for bimodal aerosol size distributions in Section 4.2.

We also show the spectral curvature (a_2) as a function of the effective radius for monomodal aerosol size distributions in Figure 4b. Note that the curvature is always negative for size distributions typical of fine mode aerosols ($R_{eff} \lesssim 0.25\,\mu$m). The curvature can become positive at larger radii, but the transition radius from negative to positive curvature is dependent upon the width (σ) of the distribution. We explore the impact of coarse mode aerosols on the curvature of bimodal aerosol size distributions further in Section 5.

4.2. Bimodal aerosol size distributions

Atmospheric aerosols are rarely monomodal [*Whitby*, 1978], so Figure 4a is of limited value for understanding the relationship between atmospheric aerosol size distributions and the Angstrom exponent. Hence, we repeated our calculations, this time limiting the fine mode median radius from 0.06 to 0.3 μm and including a coarse mode with $R_{crs} = 3.2\,\mu$m and $\sigma_{crs} = 0.75$. We also varied the ratio of the concentration of aerosols in the fine mode to the combined aerosol concentration $[C_{fine}/(C_{fine} + C_{crs})]$ from 0.1 to 1, scaling both modes as necessary to maintain a normalized optical thickness at $\lambda = 0.44\,\mu$m. The results are shown in Figure 5, where we have defined the fine mode effective radius as the effective radius for the distribution of particles with radii less than 0.6 μm (the mode separation radius recommended by AERONET at http://aeronet.gsfc.nasa.gov).

The uppermost line in Figure 5 represents a monomodal aerosol size distribution and is a subset of the line in Figure 4a with $\sigma = 0.38$. The lines below the uppermost line in Figure 5 represent the influence of including various concentrations of coarse mode aerosols. The figure indicates that increasing the concentration of coarse mode particles (i.e., $C_{fine}/C_{total} \downarrow$) reduces the Angstrom exponent and dampens its sensitivity to the fine mode effective radius. This latter point is evidenced by the reduction in the slope of the C_{fine}/C_{total} lines with decreasing C_{fine}/C_{total} at fine mode effective radii common to atmospheric aerosols (i.e., $0.1 \lesssim R_{eff}(fine) \lesssim 0.25\,\mu$m). This reduction in slope occurs because we are adding coarse mode particles with spectrally flat extinctions to our system of particles, reducing the overall spectral variability .

It is also evident in Figure 5 that an increase in the Angstrom exponent does not necessarily correspond to a decrease in the fine mode effective radius. For instance, a bimodal size distribution with $C_{fine}/C_{total} = 0.8$ and $R_{eff}(fine) = 0.07\,\mu$m has an Angstrom exponent of $\alpha = 2.1$ in Figure 5, but the same modal concentration ratio and a fine mode effective radius of $R_{eff}(fine) = 0.09\,\mu$m has an Angstrom exponent of 2.4. This is contrary to the conventional wisdom of Figure 4, which holds that the Angstrom exponent *decreases* with increasing particle size (all else being equal). This "unconventional" behavior shown in Figure 5 occurs because the coarse mode exhibits a strong influence on the Angstrom exponent when added to distributions composed of the least efficient particles (i.e., the smallest ones). The fine mode extinction becomes more efficient as the fine mode effective radius increases beyond the smallest values shown in Figure 5 , however, and the conventional Angstrom exponent behavior appears once again (i.e., α decreases as R_{eff} increases).

5. Response of spectral curvature to changes in polydisperse aerosol parameters

Recall that the traditional powerlaw for aerosol extinction is strictly an empirical relationship (Equation 1), and that the wavelength dependence of aerosol extinction is more accurately described using a 2nd-order polynomial (Equation 7). Hence, we repeat our study of the wavelength-dependence of bimodal lognormal aerosol size distributions by once again calculating the extinction of spherical aerosols at seven wavelengths (via Equations 3 and 4), this time determining the empirical coefficients a_0, a_1, and a_2 of Equation (7) through polynomial regression. We tested bimodal size distributions with all permutations of mode sizes, widths, concentrations, and refractive indices shown in Table 1 (although we always assumed the same refractive index for both the fine and coarse modes). The parameters in Table 1 are based upon the range of AERONET climatologies of *Dubovik et al.* [2002]. Our results for this plethora of distributions are shown as the small points Figure 6. The circles correspond to the bimodal parameters used to calculate the grid of Figure 5 (**boldprint** values in Table 1), with the size of the circles corresponding to the fine mode median radii. The color of the points and the circles indicate the volume fraction of aerosols in the bimodal distribution with radii less than 0.6 μm, V_{fine}/V_{total}. The black lines approximate isolines of constant C_{fine}/C_{total}.

We first comment on the color scheme shown in Figure 6, which is coded to represent the volume fraction of aerosols with radii less than 0.6 μm. Note that V_{fine}/V_{total} is not necessarily equivalent to C_{fine}/C_{total}; V_{fine}/V_{total} is the volume fraction of aerosols in the size distribution with $r < 0.6\,\mu$m, and C_{fine}/C_{total} is defined by Equation (3). One difference between these two definitions is that the fine and coarse mode aerosol sizes

described by Equation (3) can overlap, whereas the volume fractions V_{fine} and V_{total} can not overlap in size because of the hard cut-off at $r = 0.6\,\mu$m. We chose this nomenclature for the color code because real atmospheric aerosols are not necessarily constrained by Equation (3), and $r = 0.6\,\mu$m is the fine/coarse mode separation radius recommended by AERONET (http://aeronet.gsfc.nasa.gov). Also note that the color transitions (i.e., from blue to green to orange, etc.) in Figure 6 are roughly parallel to the black lines. This is because all lines of constant V_{fine}/V_{total} or C_{fine}/C_{total} calculated from the parameters in Table 1 have the same general shape. Hence, conclusions about the size distributions represented by the circles in Figure 6 can be generalized to all size distributions in Table 1.

Next, we point the reader to the monomodal size distributions in Figure 6 (red circles to the right, with $C_{fine}/C_{total} = 1$). In this case, we see that the curvature is always negative ($a_2 < 0$) and that it decreases as particle size increases; we found this to be true for all cases with $C_{fine}/C_{total} = 1$ in Table 1. Positive curvature requires the presence of enough coarse mode aerosols to reduce the wavelength dependence of aerosol extinction at the longer wavelengths (recall Figure 3). Note that negative curvature can be achieved even with the presence of a significant coarse mode component, as evidence by the blue points below the $a_2 = 0$ line.

Also note that the absolute value of the coefficient a_1 decreases with increasing particle size for the fine monomodal aerosols with $C_{fine}/C_{total} = 1$, much like its near cousin α (recall that the rightmost red circles in Figure 6 are calculated with the same nine size distributions as the uppermost line in Figure 5). This is not the case when significant coarse mode aerosols are present and the curvature is positive, as shown by the C_{fine}/C_{total}

isolines when $a_2 > 0$ in Figure 6. This is because positive curvature indicates that the coarse mode is already significantly reducing the Angstrom exponent, and increasing the effective radius of the fine mode under these conditions increases the radiative efficiency of that mode. Hence, the coefficient a_1 shifts from the low magnitudes that are associated with coarse mode aerosols to the large magnitudes that are associated with fine mode aerosols along the C_{fine}/C_{total} isolines with $a_2 > 0$. Finally, we reiterate that the curvature exhibited in Figure 6 is always negative for the size distributions of Table 1 when the coarse mode is not present.

The situation where $a_2 = 0$ corresponds to a special case without curvature, and $a_1 = -\alpha$. It is sometimes postulated that aerosol size distributions without curvature are "Junge" distributions (Equation 2), but the large number of points on or near the zero line of a_2 in Figure 6 indicate that it is possible to have bimodal lognormal aerosol size distributions without curvature. The size of the circles and color of the points on the line $a_2 = 0$ in Figure 6 are also consistent with conventional wisdom about the Angstrom exponent (i.e., they indicate that the fine mode median radius decreases and the fine mode volume fraction increases as $|a_1|$ increases).

Note that a_1 can be significantly different from α, and that the information content of sunphotometry measurements can be enhanced by considering the spectral curvature of extinction. For instance, recall the demonstration of Figure 3, where extinction calculations for two plausible aerosol size distributions produced the same Angstrom exponent. One size distribution was monomodal with a fine mode median radius of $R_{fine} = 0.21$ and width of $\sigma = 0.38$, and the other distribution was bimodal with a fine mode fraction of $C_{fine}/C_{total} = 0.6$, $\sigma_{fine} = 0.38,$ and $\sigma_{crs} = 0.75$. Both of these size distributions produce

an Angstrom exponent of $\alpha = 2.0$, but they produce measurably different coefficients when curvature is considered. Both size distributions can be located by the appropriate black squares in Figure 6, revealing that $(a_1, a_2) = (-2.78, -0.76)$ for the monomodal distribution, and $(a_1, a_2) = (-1.74, +0.26)$ for the bimodal distribution.

To a close approximation, $\alpha = a_2 - a_1$; hence, we have included two dashed lines in Figure 6 that represent the traditional guidelines for the Angstrom exponent. Lines of constant α run parallel to these lines (not shown). Figure 6 indicates that $a_2 - a_1 \gtrsim 2$ corresponds to size distributions dominated by fine mode aerosols and $a_2 - a_1 \lesssim 1$ corresponds to size distributions dominated by coarse mode aerosols, as expected. Intermediate values of $a_2 - a_1$ (or α) correspond to a wide range of fine mode fractions.

6. A word about absorption

The computations shown in Figure 6 represent a single imaginary refractive index of $m_i = 0.003$, or a single bulk absorption coefficient. Natural aerosols have a variety of bulk absorption coefficients, however, so we demonstrate the sensitivity of the Angstrom exponent to a range of imaginary refractive indices in Figure 7. We used $m_i = 10^{-6}$ to simulate aerosols with negligible absorption and $m_i = 0.02$ to simulate extremely absorbing aerosols (in addition to our previous value of $m_i = 0.003$). We show results for three lognormal fine mode fractions of $\frac{C_{fine}}{C_{total}} = 0.1, 0.3,$ and 0.8.

Figure 7 indicates that the Angstrom exponent is not sensitive to the bulk absorption coefficient for the two lowest lognormal fine volume fractions (i.e., $\frac{C_{fine}}{C_{total}} = 0.1$ and 0.3). We can understand this by noting that $\alpha \lesssim 1$ at these volume fractions, and recalling that the spectral absorption of small particles is often approximated as $\tau_{abs} \propto \lambda^{-1}$ [*Bergstrom*, 2002]. Since the spectral dependence of absorption is similar to the spectral dependence

of extinction for coarse mode particles, the bulk absorption coefficient has little effect on the extinction exponent of these particles. However, the bulk absorption coefficient does have an impact on the Angstrom exponent for large volume fractions of fine mode aerosols (i.e., $\frac{C_{fine}}{C_{total}} = 0.8$ in Figure 7). Note that the sensitivity is small, though, as the extreme variability of m_i in Figure 6 produces a maximum change in α of 0.3 at $\frac{C_{fine}}{C_{total}}) = 0.8$.

7. Implications for measurements

Thus far, we have only discussed the calculated spectral dependence of aerosol extinction for hypothetical size distributions of idealistic spherical aerosols. The question arises: How does this information convey into real world measurements? Fortunately, we have the Aerosol Robotics Network (AERONET) of narrow field of view radiometers, which provides aerosol optical depth measurements at over 180 locations worldwide [*Holben et al.*, 1998, 2001]. Additionally, the AERONET radiometers periodically perform sky radiance scans which enable the retrieval of column-averaged aerosol size distributions and refractive indices [*Dubovik and King*, 2000; *Dubovik et al.*, 2000]. In this section, we use data from the Aerosol Robotics Network (AERONET) of surface radiometers to further illustrate the relationships between the Angstrom exponent, curvature, fine mode volume fraction, and fine mode effective radius.

We begin our discussion with Figure 8, which shows the fine mode volume fractions (upper panel) and fine mode effective radii (lower panel) obtained from AERONET size distribution retrievals at 53 locations in the years 2000 and 2001 as a function of the Angstrom exponent. The AERONET size distributions are provided as column concentrations at 22 radii and not necessarily constrained by Equation (3), so we use the nomenclature V_{fine}/V_{total} to denote the volume fraction of aerosols with radii less than 0.6 μm.

We calculated the Angstrom exponents and curvatures in Figure 8 from multi-wavelength AOT measurements ($\lambda = 0.34, 0.38, 0.44, 0.5, 0.67, 0.87,$ and $1.02\,\mu$m) using least squares fits of Equations (6) and (7). We only considered AERONET retrievals with aerosol optical thicknesses greater than 0.2 at the 0.44 μm wavelength and a real refractive index difference of less than 0.1 between the 0.44 and 1.020 μm wavelengths. We also present the Angstrom exponent calculations used in Figure 5 as solid lines in the lower panel of Figure 8 (note that the variables in the lower panel of Figure 8 are the same as Figure 5, with the ordinate and abscissa interchanged).

Momentarily ignoring the color scheme in Figure 8, we see that the multi-wavelength Angstrom exponent provides at least some information about the volume fraction of aerosols in the fine mode, but little or no information about the fine mode effective radius. For instance, the upper panel of Figure 8 indicates Angstrom exponents greater than 2 correspond to fine mode volume fractions greater than about 0.5, Angstrom exponents less than 1 correspond to fine mode volume fractions less than about 0.5, and that intermediate values for α correspond to fine volume fractions of 0.2–0.85. This is consistent with conventional wisdom that size distributions with large Angstrom exponents are dominated by fine mode particle sizes. However, the lower panel of Figure 8 indicates no relationship between the Angstrom exponent and the fine mode effective radius.

The color scheme of Figure 8 indicates that including spectral curvature in our analysis may enhance our knowledge about the volume fraction and effective radius of fine mode aerosols at intermediate values of the Angstrom exponent ($1 \lesssim \alpha \lesssim 2$), which we discuss here. Suppose a value of $\alpha = 1.5$ was calculated from multi-wavelength AOTs, which we have already noted corresponds to a fine mode volume fraction range of 0.2–0.85. Paying

attention to the color scheme in Figure 8, we see that the negative curvatures favor high volume fractions and positive curvatures favor low volume fractions at this intermediate value for α. Our analysis of Figure 8 at $\alpha = 1.5$ indicates that $a_2 \lesssim -0.3$ (blue squares) corresponds to fine mode volume fractions greater than 0.4. Similarly, $a_2 \gtrsim 0.3$ (red squares) corresponds to fine mode volume fractions less than 0.65. Likewise, the largest fine mode effective radii require large negative curvatures (lower panel of Figure 8), consistent with our theoretical discussion of Section 5. Hence, the presence of curvature can be used to improve our assessment of aerosol size distributions at intermediate Angstrom exponents. Note that the curvature adds no new information for $\alpha \lesssim 1$ and $\alpha \gtrsim 2$.

We plot the same AERONET data in Figure 9, this time mimicking the format of Figure 6. The data indicate that the coefficient a_1 and the curvature a_2 tend to decrease as the fraction of particles in the fine mode increases, consistent with our theoretical plot of Figure 6. This is consistent with *Eck et al.* [1999]; *Eck. et al.* [2001b], and *Kaufman* [1993], who found that the fine mode dominates when the curvature is negative, and that the coarse mode contributes significantly when positive curvature is present. Nonetheless, the data also indicate that negative curvatures are possible for size distributions dominated by coarse mode particles (i.e., blue points below the $a_2 = 0$ line) and positive curvatures are possible for size distributions dominated by fine mode particles (red points above the $a_2 = 0$ line).

In satellite remote sensing, the retrieval of the Angstrom exponent is based upon a single pair of wavelengths [*Nakajima and Higurashi*, 1998; *Higurashi and Nakajima*, 1999; *Deuze et al.*, 2000; *Ignatov and Stowe*, 2002; *Jeong et al.*, 2005]. Conclusions about the size distribution in such cases must consider the retrieval wavelengths, as different

wavelength pairs will provide different information about the aerosol size distribution. This is demonstrated in Figure 10, where we have plotted the Angstrom exponents of two-wavelength pairs for synthetic bimodal lognormal distributions and for AERONET data. Here, the AERONET data is once again obtained from almucantar retrievals at 53 AERONET sites, and the circles are calculated from Equations (3) and (4) using the **boldprint** bimodal parameters of Table 1. The Angstrom exponents for each axis were calculated using only two wavelengths in Equation (6).

Note that the Angstrom exponent from the AERONET dataset is rarely linear, as evidenced by the small fraction of data on the 1:1 line in Figure 10. The upper panel indicates that negative curvature ($a_2 < 0$) favors larger fractions of fine mode aerosols, but fine mode volume fractions greater than 0.5 are not required for negative curvature. Likewise, the lower panel of Figure 10 indicates that positive curvature ($a_2 > 0$) favors smaller fine mode radii, but this is not always the case. Separation of colors for AERONET data would indicate that one could obtain fine volume fraction and effective radius from this type of plot, but there is considerable intermingling of colors, making detailed conclusions about the size distribution nebulous.

This is illustrated more clearly in Figure 11, where we present the same AERONET data once again. Figure 11a indicates that calculating the Angstrom exponent based upon the 0.38 and 0.44 μm wavelengths will tell us very little about the fine mode volume fraction of aerosols, as evidenced by the large amount of scatter and the small slope of the linear regression. This is because both of these wavelengths are less sensitive to coarse mode aerosols than the 0.5 μm wavelength shown in Figure 1. This lack of sensitivity to the coarse mode increases the sensitivity of these wavelengths to changes in the fine mode

effective radius, as shown in Figure 11b. Conversely, the Angstrom exponents based upon the 0.67 and 0.87 μm wavelengths are indeed sensitive to the fine mode volume fraction (albeit with much scatter), as shown by the slope in Figure 11c, and have nearly no sensitivity to the fine mode effective radius (Figure 11d). This wavelength sensitivity of α is consistent with the work of others [*Eck. et al.*, 2001b; *O'Neill et al.*, 2001a; *Reid et al.*, 1999].

8. Real versus synthetic data

Note that the color transitions for the AERONET data in Figure 9 are not nearly as clean as the transitions for the synthetic data of Figure 6, which we explain in this section. Measured AOTs were used to calculate the coefficients (a_1, a_2) in Figure 9, so this is our benchmark. Nonetheless, measurement noise exists in Figure 9 that is not considered in the synthetic calculations of Figure 6. Sunphotometry measurements of AOT are typically accurate to 0.02 or better for newly calibrated field instruments [*Holben et al.*, 1998], and this uncertainty alters the Angstrom exponent α by 0.03–0.04; we can expect similar variability in a_1. This variability in a_1 (and a_2) manifests itself as an intermingling of colors in Figure 9, as does any errors associated with the AERONET size distributions retrievals. The data in Figure 6, on the other hand, are somewhat idealistic because these noise issues are not taken into consideration. We chose a single imaginary refractive index for the computations of Figure 6, which reduces the computational noise associated with the discussion of Section 5

We also chose to use χ^2 iteration to infer aerosol absorption for Figure 6, which gives a spectrally smooth and plausible refractive index for an internal mixture of ammonium sulfate, water, and black carbon. We note that using χ^2 iteration of the refractive index

with AERONET distributions (which are not necessarily lognormal) also produces an idealistic scenario similar to Figure 6 (not shown), so the shape of the size distributions is not a source of noise. We also note that we can reproduce measured AOTs to within 0.03 using the AERONET size distributions and AERONET refractive indices at the four almucantar wavelengths, so our Mie computations are correct.

Other issues besides the measurement noise are also responsible for the differences between Figures 6 and 9. Applying the χ^2 iteration procedure to the AERONET aerosol retrievals does not necessarily produce refractive indices that exactly match the AERONET refractive indices (although the magnitude of the difference is limited by the magnitude of the spectral variability of the AERONET retrieval). Aerosol optical depth calculations are very sensitive to the real refractive index, as variations in the real refractive index of 0.02 at the 0.440 μm wavelength can produce optical depth variations as large as 0.12. Spectral variations of the refractive index beyond the small spectral variability for water and ammonium sulfate will not show up in Figure 6, so some of the noise in Figure 9 could occur because of realistic spectral variations in the AERONET refractive index. Large spectral variability of the real refractive index is not expected for nondust aerosols, however. Cases where the retrieved real refractive index exhibits unrealistically large spectral variability may also indicate an erroneous fine mode fraction, since the AERONET retrieval is constrained by the AOT at the four almucantar wavelengths. Such cases would also appear as noise in Figure 9.

9. Conclusions

We have discussed the relationship between polydisperse aerosol size distributions and the spectral dependence of the aerosol optical thickness, using both Mie calculations and

AERONET aerosol retrievals. We began by showing the expected inverse relationship between the Angstrom exponent and the effective radius for synthetic monomodal aerosol size distributions.

Next, we discussed the sensitivity of the Angstrom exponent and curvature to the details associated with bimodal aerosol size distributions, focusing specifically on the fine mode effective radius and the fine mode fraction of aerosols. We demonstrated that calculations of the Angstrom exponent for seven wavelengths (0.34, 0.38, 0.44, 0.50, 0.67, 0.87, and 1.02 μm) are sensitive to the fraction of aerosols in the fine mode (V_{fine}/V_{total}), but not to the fine mode effective radius ($R_{eff}(fine)$). Nonetheless, this multi-wavelength Angstrom exponent is not a rigorous indicator of V_{fine}. Rather, AERONET retrievals at approximately 50 sites indicate that $\alpha \gtrsim 2$ correspond to fine mode fractions of $V_{fine} \gtrsim 0.5$, and $\alpha \lesssim 1$ correspond to fine mode fractions of $V_{fine} \lesssim 0.5$. The same AERONET dataset indicates that intermediate values of α correspond to fine mode fractions between 0.2 and 0.85, but improved estimates of the fine mode aerosol fractions can be obtained by considering the spectral curvature. For instance, if $\alpha = 1.5$, then curvatures of $a_2 \lesssim -0.3$ indicate fine mode fractions of $0.5 \lesssim V_{fine} \lesssim 0.85$, and $a_2 \gtrsim +0.3$ indicate fine mode fractions of $0.2 \lesssim V_{fine} \lesssim 0.5$. Although the curvature is useful for estimating the fine mode fraction of aerosols at intermediate values of α, it provides no additional information when $\alpha \lesssim 1$ and $\alpha \gtrsim 2$.

Spectral curvature of aerosol extinction also plays a significant role when the Angstrom exponent is calculated with only two wavelengths. Angstrom exponents calculated from longer wavelength pairs ($\lambda = 670, 870\,\mu$m) are sensitive to the fine mode fraction of aerosols but not the fine mode effective radius; conversely, shorter wavelength pairs ($\lambda =$

380, 440 μm) are sensitive to the fine mode effective radius but not the fine mode fraction (see also *Eck et al.* [1999]; *Eck. et al.* [2001b]; *Kaufman* [1993]). Hence, it is important to consider the wavelength pair used to calculate the Angstrom exponent when making qualitative assessments about the corresponding aerosol size distributions.

Acknowledgments. This work was funded by the Earth Science Enterprise, the Cloud's and the Earth's Radiant Energy System (CERES) project, and by the NASA Langley Incubator Institute program. We appreciate the efforts of the AERONET team and the instrument principle investigators for establishing and maintaining the 53 sites used in this investigation. We are also grateful to H. Garland Gouger, the NASA LaRC librarian who did an extensive search for Lindholm and Lundholm.

References

Angstrom, A. (1929), On the atmospheric transmission of sun radiation and on dust in the air, *Geografiska Annaler*, *11*, 156–166.

Angstrom, A. (1930), On the atmospheric transmission of sun radiation. II., *Geografiska Annaler*, *2*(12), 130–159.

Angstrom, A. (1961), Techniques of determining the turbidity of the atmosphere, *Tellus*, *13*(2), 214–223.

Angstrom, A. (1964), The parameters of atmospheric turbidity, *Tellus*, *XVI*(1), 64–75.

Bergstrom (2002), Wavelength dependence of the absorption of black carbon particles: Predictions and results from the TARFOX experiment and implications for the aerosol single scattering albedo, *J. Atmos. Sci.*, *59*, 567–577.

Bohren, C. (Ed.) (1989), *Selected papers on scattering in the atmosphere*, *SPIE Milestone Series*, vol. MS 7, SPIE.

Cachorro, V., and A. de Frutos (1995), A revised study of the validity of the general Junge relationship at solar wavelengths: Application to vertical atmospheric aerosol layer studies, *Atmospheric Research*, *39*, 113–126.

Cachorro, V., A. de Frutos, and M. Gonzalez (1993), Analysis of the relationships between Junge size distribution and Angstrom α turbidity parameters from spectral measurements of atmospheric aerosol extinction, *Atmos. Environ.*, *27A*(10), 1585–1591.

Cachorro, V., P. Duran, R. Vergaz, and A. de Frutos (2000), Columnar physical and radiative properties of atmospheric aerosols in north central Spain, *J. Geophys. Res.*, *105*(D6), 7161–7175.

Davies, C. (1974), Size distribution of atmospheric particles, *Aerosol Science*, *5*, 293–300.

Deuze, J., P. Goloub, M. herman, A. Marchand, and G. Perry (2000), Estimate of the aerosol properties over the ocean with polder, *J. Geophys. Res.*, *105*(D12), 15,329–15,346.

Dubovik, O., and M. King (2000), A flexible inversion algorithm for retrieval of aerosol optical properties from sun and sky radiance measurements, *J. Geophys. Res.*, *105*(D16), 20,673–20,696.

Dubovik, O., B. N. Holben, Y. J. Kaufman, M. Yamasoe, A. Smimov, D. Tanre, and I. Slutsker (1998), Single-scattering albedo of smoke retrieved from the sky radiance and solar transmittance measured from ground, *J. Geophys. Res.*, *103*(D24), 31,903–31,923.

Dubovik, O., A. Smirnov, B. Holben, M. King, Y. Kaufman, T. Eck, and I. Slutsker (2000), Accuracy assessments of aerosol optical properties retrieved from Aerosol Robotic Network (AERONET) sun and sky radiance measurements, *J. Geophys. Res.*, *105*(D8), 9791–9806.

Dubovik, O., B. Holben, T. Eck, A. Smirnov, Y. Kaufman, M. King, D. Tanre, and I. Slutsker (2002), Variability of absorption and optical properties of key aerosol types observed in worldwide locations, *J. Atmos. Sci.*, *59*, 590–608.

Eck, T., B. N. Holben, J. Reid, O. Dubovik, A. Smirnov, N. O'Neill, I. Slutsker, and S. Kinne (1999), Wavelength dependence of the optical depth of biomass burning, urban, and desert dust aerosols, *J. Geophys. Res.*, *104*(D24), 31,333–31,349.

Eck., T., B. N. Holben, O. Dubovik, A. Smirnov, I. Slutsker, J. Lobert, and V. Ramanathan (2001a), Column-integrated aerosol optical properties over the Maldives during the northeast monsoon for 1998–2000, *J. Geophys. Res.*, *106*(D22), 28,555–28,566.

Eck., T., et al. (2001b), Characterization of the optical properties of biomass burning aerosols in Zambia during the 1997 ZIBBEE field campaign, *J. Geophys. Res.*, *106*(D4), 3425–3448.

Eck., T., et al. (2003), Variability of biomass burning aerosol optical characteristics in southern Africa during the SAFARI 2000 dry season campaign and a comparison of single scattering albedo estimates from radiometric measurements, *J. Geophys. Res.*, *108*(D13), 8477, doi:10.1029/2002JD002321.

Hansen, J., and L. Travis (1974), Light scattering in planetary atmospheres, *Space Sci. Rev.*, *16*, 527–610.

Higurashi, A., and T. Nakajima (1999), Development of a two-channel aerosol retrieval algorithm on a global scale using NOAA AVHRR, *J. Atmos. Sci.*, *56*, 924–941.

Holben, B., et al. (1998), AERONET – A federated instrument network and data archive for aerosol characterization, *Remote Sens. Environ.*, *66*, 1–16.

Holben, B., et al. (2001), An emerging ground-based aerosol climatology: Aerosol optical depth from AERONET, *J. Geophys. Res.*, *106*(D11), 12,067–12,097.

Ignatov, A., and L. Stowe (2002), Aersol retrievals from individual AVHRR channels. part I: Retrieval algorithm and transistion from Dave to 6S radiative transfer model, *J. Atmos. Sci.*, *59*, 313–334.

Jeong, M., Z. Li, D. Chu, and S. Tsay (2005), Quality and compatibility analyses of global aerosol products derived from the advanced very high resolution radiometer and moderate resolution imaging spectroradiometer, *J. Geophys. Res.*, *110*, D10S09, doi: 10.1029/2004JD004648.

Junge, C. (1955), The size distribution and aging of natural aerosols as determined from electrical and optical data in the atmosphere, *J. Appl. Meteorol.*, *12*, 13–25.

Junge, C. (1963), *Air chemistry and radioactivity*, *International Geophysics Series*, vol. 4, Academic Press.

Kaufman, Y. (1993), Aerosol optical thickness and path radiance, *J. Geophys. Res.*, *98*(D2), 2677–2692.

Kaufman, Y., A. Gitelson, A. Karnieli, E. Ganor, R. Fraser, T. Nakajima, S. Mattoo, and B. N. Holben (1994), Size distribution and scattering phase function of aerosol particles retrieved from sky brightness measurements, *J. Geophys. Res.*, *99*(D5), 10,341–10,356.

Kaufman, Y., A. Smirnov, B. N. Holben, and O. Dubovik (2001), Baseline maritime aerosol: methodology to derive the optical thickness and scattering properties, *Geophys. Res. Lett.*, *28*(17), 3251–3254.

King, M., and D. Byrne (1976), A method for inferring total ozone content from the spectral variation of total optical depth obtained with a solar radiometer, *J. Atmos. Sci.*, *33*, 2242–2251.

King, M., D. Byrne, B. Herman, and J. Reagan (1978), Aerosol size distributions obtained by inversion of spectral optical depth measurements, *J. Atmos. Sci.*, *35*, 2153–2167.

Liou, K. (1992), *Radiation and cloud processes in the atmosphere*, no. 20 in Oxford monographs on geology and geophysics, Oxford University Press.

McCartney, E. (1976), *Optics of the atmosphere: scattering by molecules and particles*, Wiley.

Measures, R. (1984), *Laser remote sensing fundamentals and application*, Krieger.

Mishchenko, M., L. Travis, R. Kahn, and R. West (1997), Modeling phase functions for dustlike tropospheric aerosols using a shape mixture of randomly oriented polydisperse spheroids, *J. Geophys. Res.*, *102*(D14), 16,831–16,847.

Nakajima, T., and A. Higurashi (1998), A use of two-channel radiances for an aerosol characterization from space, *Geophys. Res. Lett.*, *25*(20), 3815–3818.

O'Neill, N., and A. Royer (1993), Extraction of bimodal aerosol-size distribution radii from spectral and angular slope (Angstrom) coefficients, *Appl. Opt.*, *32*(9).

O'Neill, N., O. Dubovik, and T. Eck (2001a), Modified Angstrom exponent for the characterization of submicrometer aerosols, *Appl. Opt.*, *40*(15), 2368–2375.

O'Neill, N., T. Eck, B. Holben, A. Smimov, and O. Dubovik (2001b), Bimodal size distribution influences on the variation of angstrom derivatives in spectral and optical depth space, *J. Geophys. Res.*, *106*(D9), 9787–9806.

O'Neill, N., T. Eck, A. Smirnov, B. N. Holben, and S. Thulasiraman (2003), Spectral discrimination of coarse and fine mode optical depth, *J. Geophys. Res.*, *108*(D17), 4559, doi:10.1029/2002JD002975.

Ott, W. (1990), A physical explanation of the lognormality of pollutant concentrations, *J. Air Waste Manage. Assoc.*, *40*, 1378–1383.

Pruppacher, H., and J. Klett (1997), *Microphysics of clouds and precipitation*, Kluwar Academic Publishers.

Reid, J., T. Eck, S. Christopher, P. Hobbs, and B. N. Holben (1999), Use of the Angstrom exponent to estimate the variability of optical and physical properties of aging smoke particles in Brazil, *J. Geophys. Res.*, *104*(D22), 27,473–27,489.

Schuster, G. L., O. Dubovik, B. N. Holben, and E. E. Clothiaux (2005), Inferring black carbon content and specific absorption from Aerosol Robotic Network AERONET aerosol retrievals, *J. Geophys. Res.*, *110*, D10S17, doi:10.1029/2004JD004548.

Seinfeld, J., and S. Pandis (1998), *Atmospheric Chemistry and Physics: From Air Pollution to Climate Change*, Wiley.

Shaw, G., J. Reagan, and B. Herman (1973), Investigations of atmospheric extinction using direct solar radiation measurements made with a multiple wavelength radiometer, *J. Appl. Meteorol.*, *12*, 374–380.

Smirnov, A., B. N. Holben, Y. Kaufman, O. Dubovik, T. Eck, I. Slutsker, C. Pietras, and R. Halthore (2002), Optical properties of atmospheric aerosol in maritime environments,

J. Atmos. Sci., *59*, 4802.

Smirnov, A., B. N. Holben, T. Eck, O. Dubovik, and I. Slutsker (2003), Effect of wind speed on columnar aerosol optical properties at Midway Island, *J. Geophys. Res.*, *108*(D24), doi:10.1029/2003JD003879.

Stephens, G. (1994), *Remote sensing of the lower atmosphere*, Oxford University Press.

Tomasi, C., E. Caroli, and V. Vitale (1983), Study of the relationship between Angstrom's wavelength exponent and Junge particle size distribution exponent, *J. Climate Appl. Meteor.*, *22*, 1707–1716.

Villevalde, Y., A. Smirnov, N. O'Neill, S. Smyshlyaev, and V. Yakovlev (1994), Measurement of aerosol optical depth in the Pacific Ocean and the North Atlantic, *J. Geophys. Res.*, *99*(D10), 20,983–20,988.

Westphal, D., and O. Toon (1991), Simulations of microphysical, radiative, and dynamical processes in a continental-scale forest fire smoke plume, *J. Geophys. Res.*, *96*(D12), 22,379–22,400.

Whitby, K. (1978), The physical characteristics of sulfur aerosols, *Atmos. Environ.*, *12*, 135–159.

Wiscombe, W. (1980), Improved mie scattering algorithms, *Appl. Opt.*, *19*(9), 1505–1509.

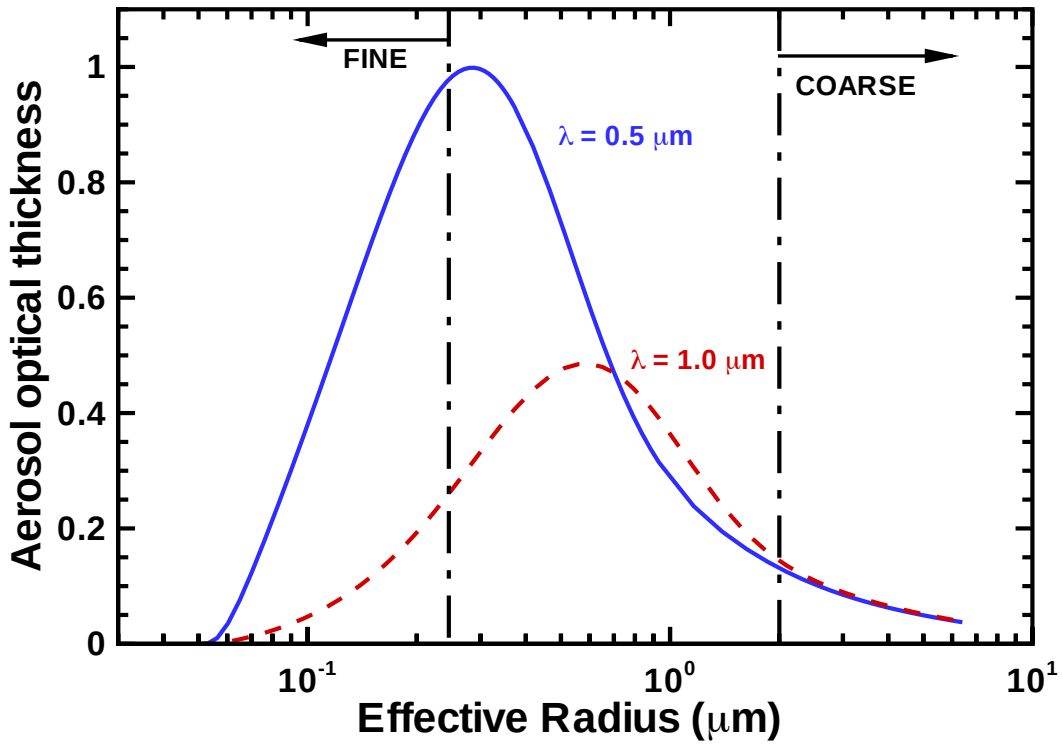

Figure 1. Relative optical thickness for monomodal distributions of aerosols described by Equation (3) with constant C_1, $C_2 = 0, \sigma_1 = 0.38$, and variable effective radii.

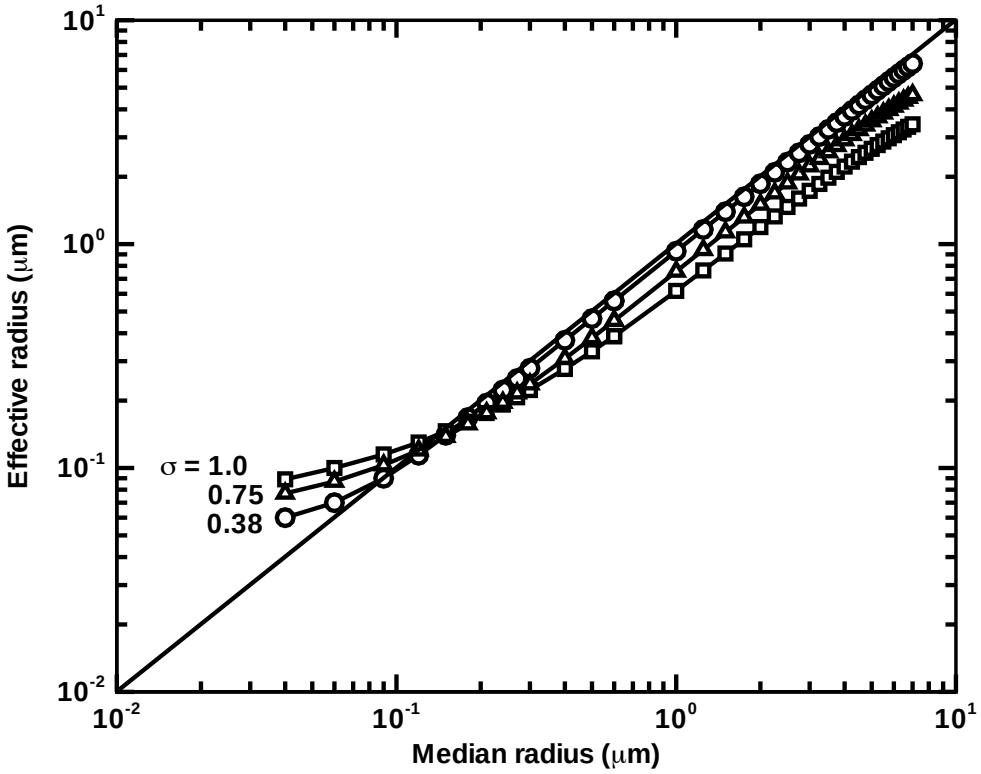

Figure 2. Relationship between the effective radius and the modal median radius of Equation (3). The discrepancy between effective radius and modal median radius increases as the mode width increases.

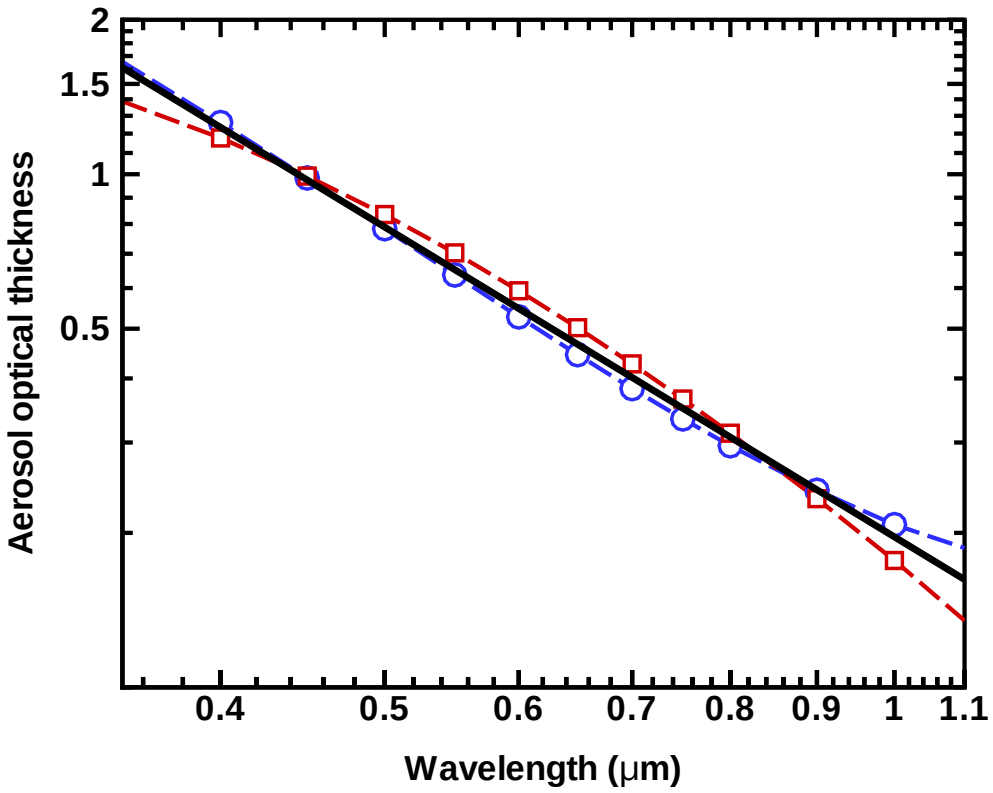

Figure 3. Spectral extinction for two different size distributions with the same Angstrom exponent ($\alpha = 2$). The squares correspond to a monomodal lognormal size distribution with $R_{fine} = 0.21$ and $\sigma = 0.38$; the circles correspond to a bimodal lognormal size distribution with $C_{fine}/C_{total} = 0.6$, $R_{fine} = 0.12, R_{crs} = 3.2, \sigma_{fine} = 0.38$, and $\sigma_{crs} = 0.75$. A refractive index of $m = 1.37 - 0.003i$ was used in both cases.

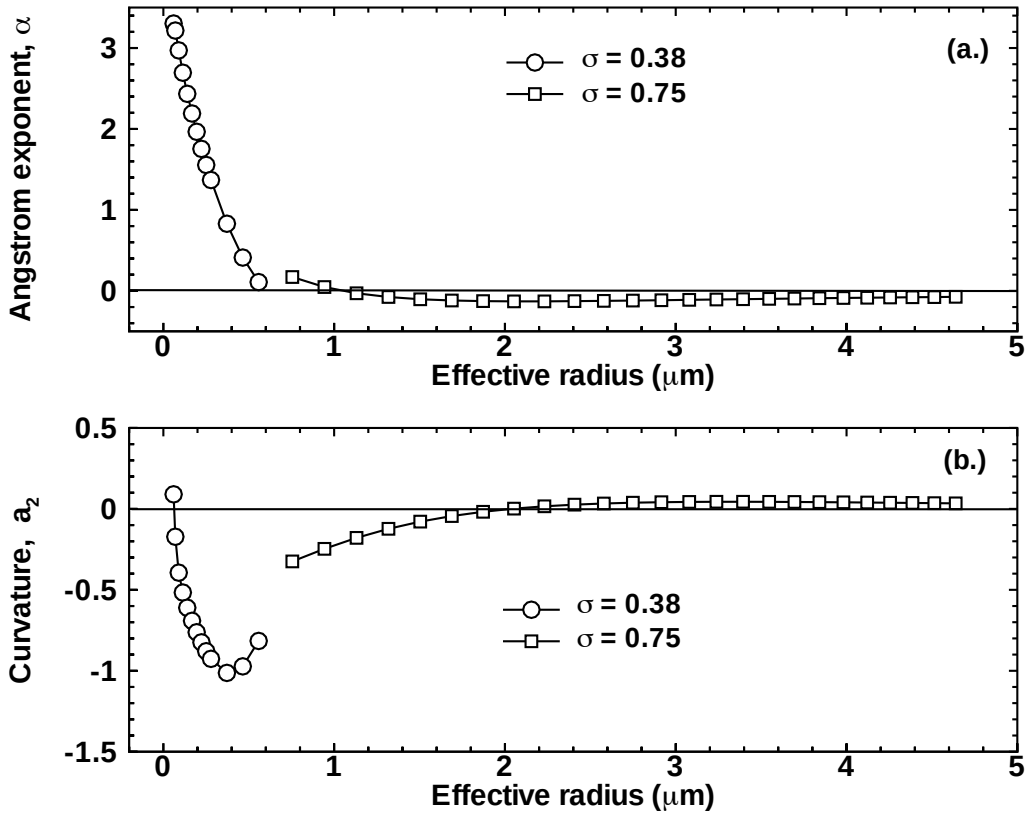

Figure 4. The Angstrom exponent (upper panel) and curvature (lower panel) for monomodal lognormal aerosol size distributions with varying effective radii. The Angstrom exponent is sensitive to fine monomodal aerosol size distributions ($R_{eff} \lesssim 0.25\,\mu$m), but not to coarse monomodal aerosol size distributions ($R_{eff} \gtrsim 2\,\mu$m). The curvature is negative for fine monomodal aerosols.

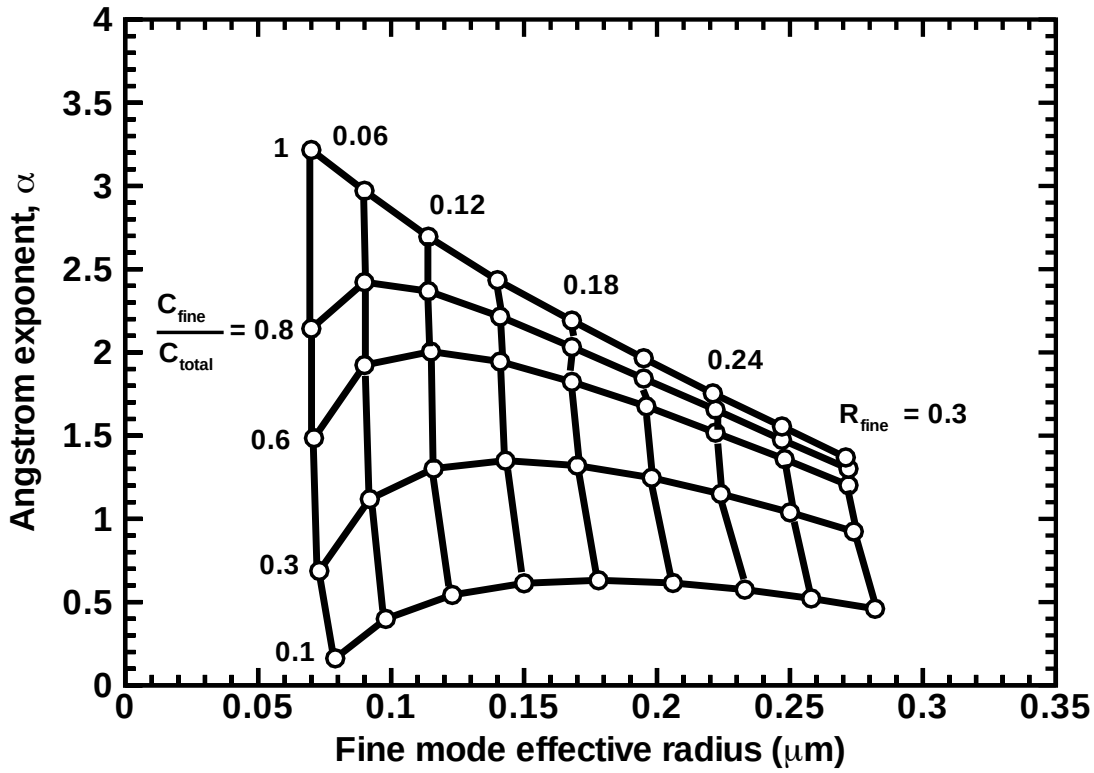

Figure 5. Calculated Angstrom exponents for bimodal aerosol size distributions using five fine mode fractions and nine fine mode median radii in Equation (3). The coarse mode radius was held constant at $R_{crs} = 3.2\,\mu$m and the mode widths were held constant at $\sigma_{fine} = 0.38$, $\sigma_{crs} = 0.75$, and the refractive index is $m = 1.37 - 0.003i$ for both modes. These parameters are listed in **boldprint** in Table 1.

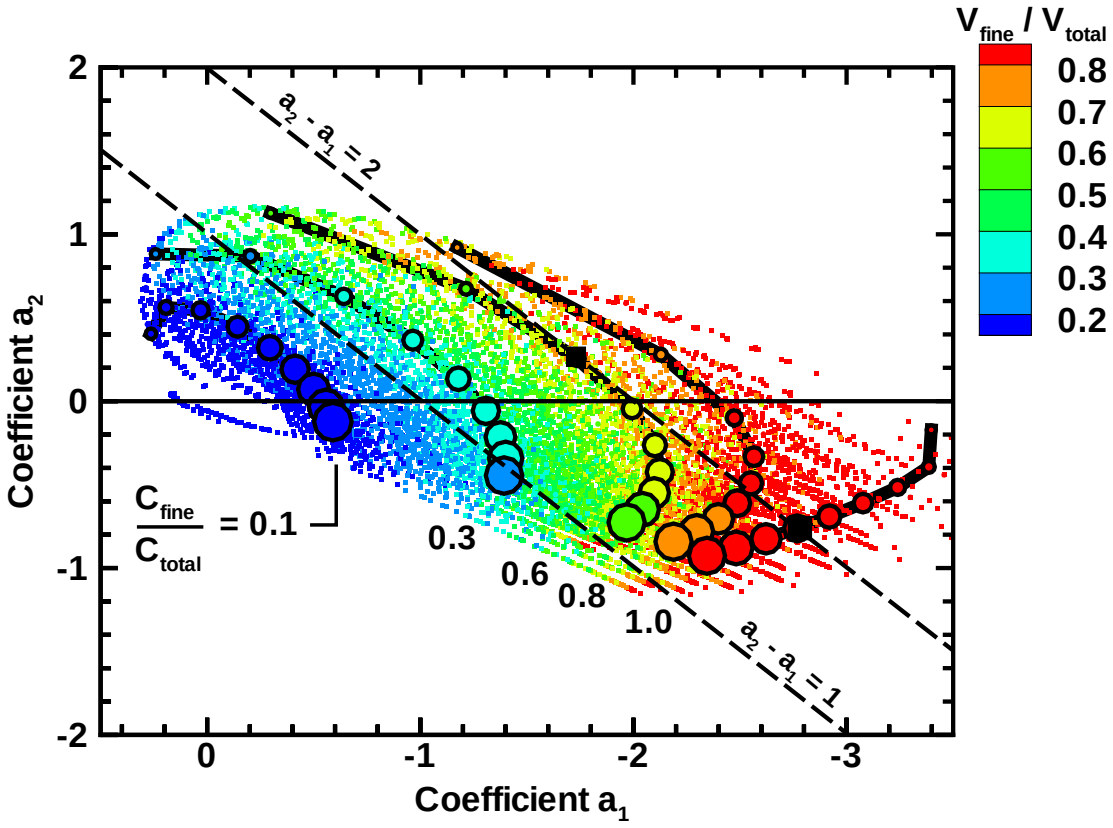

Figure 6. Volume fraction of fine mode aerosols as a function of the coefficients a_1 and a_2 in Equation (7) for 13,860 bimodal aerosol size distributions parameterized with the values in Table 1. The circles correspond to the **boldprint** values in Table 1 and are sized relative to the fine mode radius. The black squares correspond to the two size distributions with $\alpha = 2$ used in Figure 3. The dashed lines closely approximate lines of constant α.

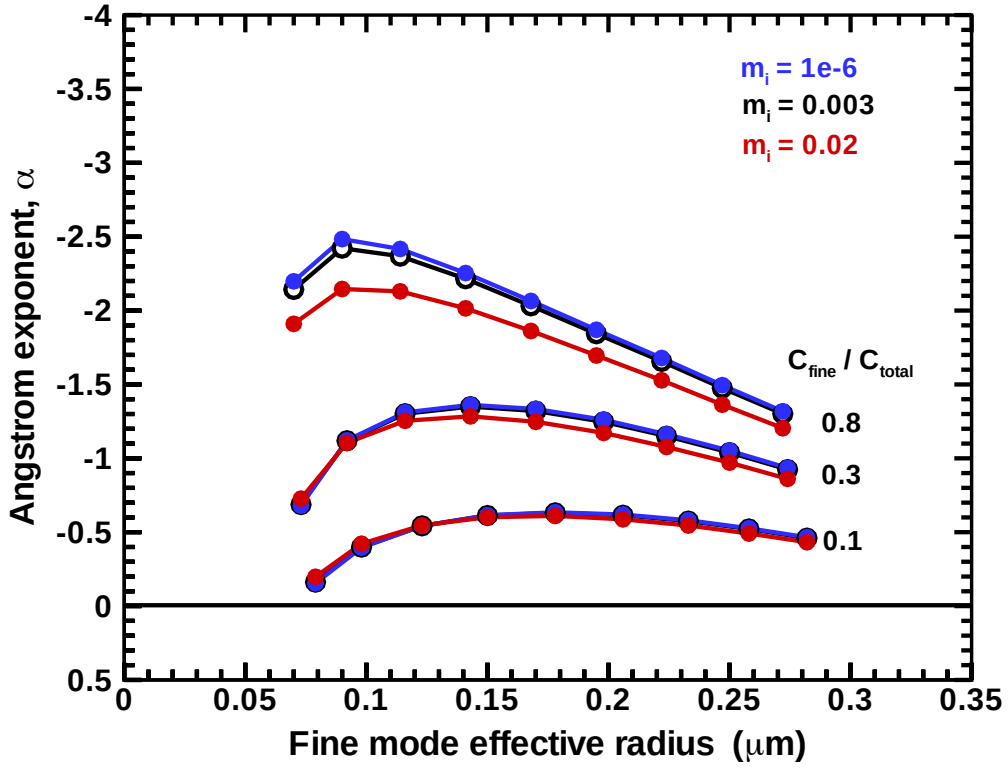

Figure 7. Sensitivity of Angstrom exponent to the aerosol imaginary refractive index (or equivalently, the bulk absorption coefficient) for bimodal aerosol distributions with three different fine volume fractions. The Angstrom exponent shows some sensitivity to absorption when the bimodal size distribution is dominated by fine mode aerosols ($\frac{C_{fine}}{C_{total}} = 0.8$), but shows virtually no sensitivity to absorption at the smaller fine mode aerosol fractions.

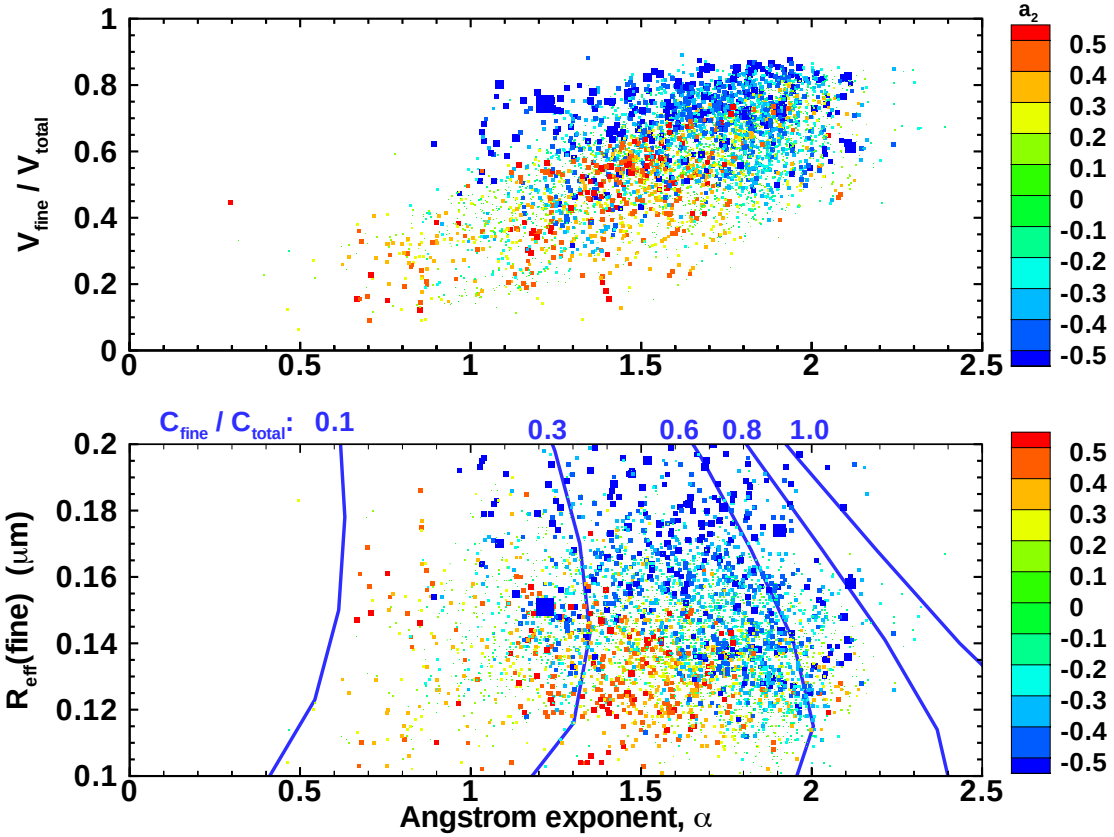

Figure 8. Fine volume fraction and fine mode effective radius as a function of the multi-wavelength Angstrom exponent. Squares correspond to AERONET almucantar retrievals and coincident AOTs at 53 locations in the years 2000 and 2001; the color of the squares correspond to the spectral curvature of the sunphotometry measurements, and the size of the squares correspond to the magnitude of the curvature, $|a_2|$. Lines in the lower panel represent constant C_{fine}/C_{total} values for bimodal lognormal aerosol size distributions parameterized with the **boldprint** values in Table 1.

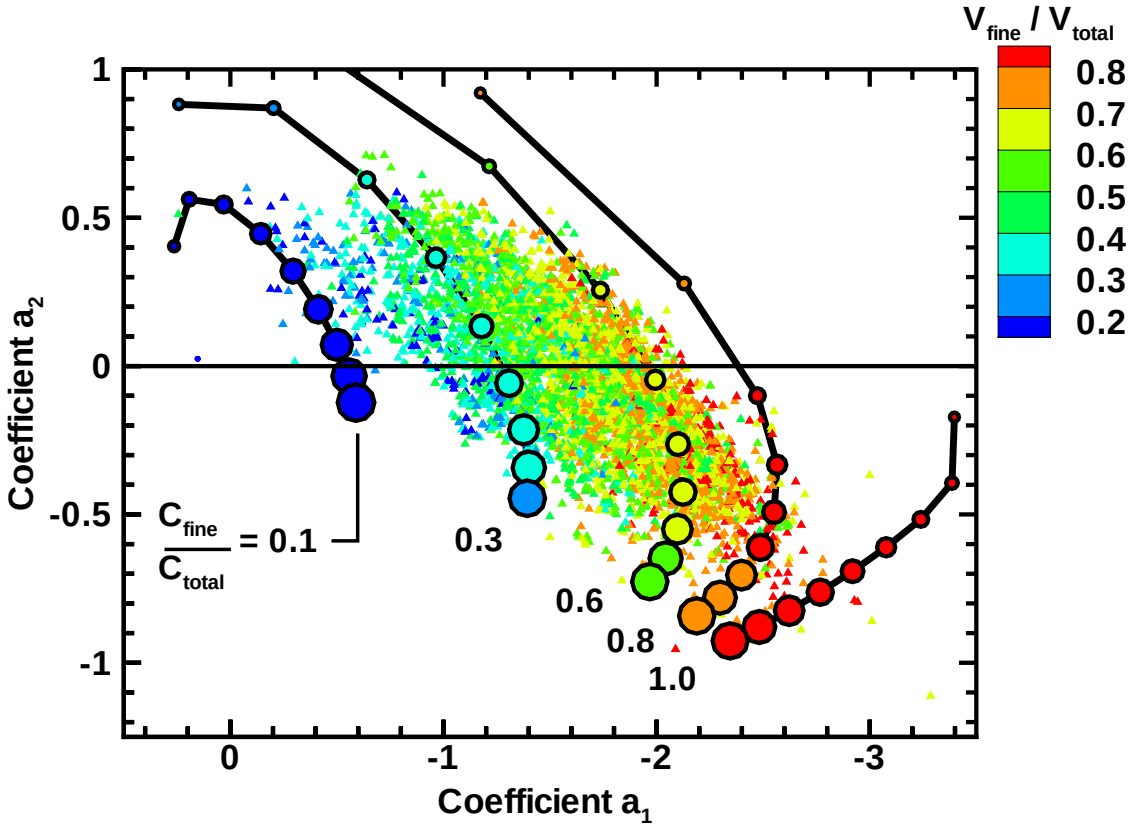

Figure 9. Same as Figure 6, except that the small points indicate the fine volume fractions obtained from AERONET retrievals.

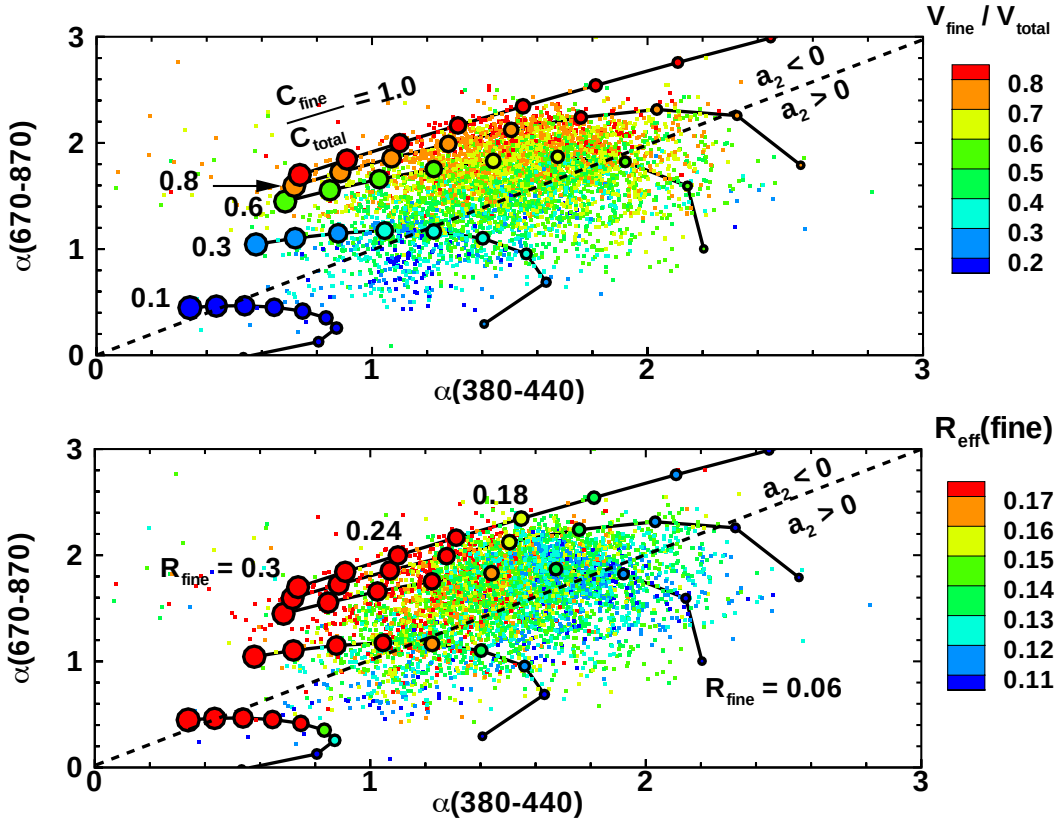

Figure 10. Fine mode volume fraction (upper panel) and fine mode effective radius (lower panel) as a function of two-wavelength Angstrom exponents. Small points are sunphotometry data from 53 AERONET sites. Circles are synthetic lognormals with **boldprint** values in Table 1, with sizes proportional to the fine mode median radius. Shorter wavelength Angstrom exponents are more sensitive to fine mode particle size than longer wavelength Angstrom exponents; longer wavelength Angstrom exponents are more sensitive to fine volume fraction than shorter wavelength Angstrom exponents.

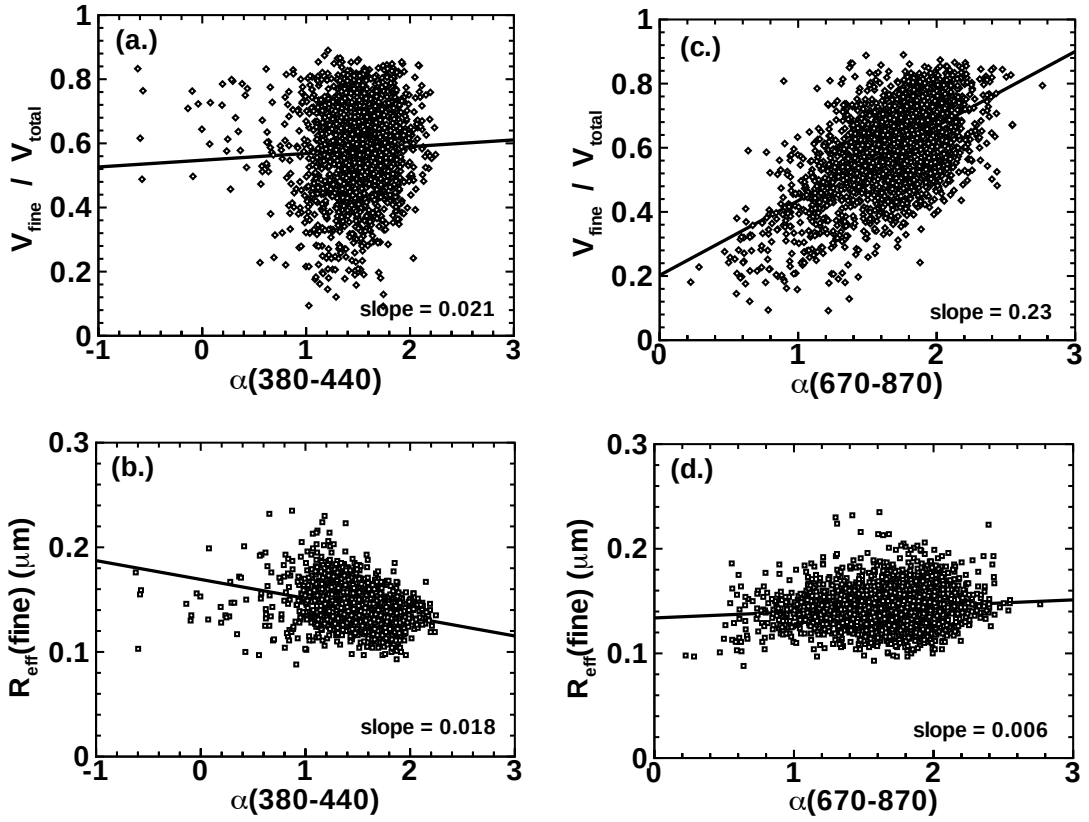

Figure 11. Fine mode volume fraction and fine mode effective radius as a function of the 380–440 two-wavelength Angstrom exponent (left panels) and the 670–870 two-wavelength Angstrom exponent (right panels). A comparison of the linear regression slopes in each panel indicates that the long wavelength Angstrom exponent has greater sensitivity to the fine mode aerosol fraction than the short wavelength Angstrom exponent (upper panels). Likewise, the short wavelength Angstrom exponent has greater sensitivity to the fine mode effective radius than the long wavelength Angstrom exponent (lower panels)).

Table 1. Bimodal lognormal size distribution parameters used to calculate the points in Figures 6 and 10. Values in **boldprint** are also used to calculate the circles in Figures 5–10.

Parameter	**Value**
$R_{fine}(\mu\mathrm{m})$	**0.06, 0.09, 0.12, 0.15, 0.18, 0.21, 0.24, 0.27, 0.30**
σ_{fine}	**0.38**, 0.5
$R_{crs}(\mu\mathrm{m})$	1.9, 2.2, 2.7, **3.2**, 3.7
σ_{crs}	**0.75**, 1.0
m_r	1.34, **1.37**, 1.4, 1.43, 1.47, 1.5, 1.54
m_i	**0.003**
C_{fine}/C_{total}	0.0, **0.1**, 0.2, **0.3**, 0.4, 0.5, **0.6**, 0.7, **0.8**, 0.9, **1.0**